




## Article

# A Reversible Optical Sensor Film for Mercury Ions Discrimination Based on Isoxazolidine Derivative and Exhibiting pH Sensing

Reham Ali <sup>1,2</sup> , Siwar Ghannay <sup>1</sup>, Sabri Messaoudi <sup>1,3</sup>, Fahad M. Alminderej <sup>1</sup> , Kaïss Aouadi <sup>1,4</sup> and Sayed M. Saleh <sup>1,5,\*</sup> 

<sup>1</sup> Department of Chemistry, College of Science, Qassim University, Buraidah 51452, Saudi Arabia

<sup>2</sup> Chemistry Department, Faculty of Science, Suez University, Suez 43518, Egypt

<sup>3</sup> Faculty of Sciences of Bizerte, Carthage University, Bizerte 7021, Tunisia

<sup>4</sup> Faculty of Science of Monastir, University of Monastir, Avenue of the Environment, Monastir 5019, Tunisia

<sup>5</sup> Chemistry Branch, Department of Science and Mathematics, Faculty of Petroleum and Mining Engineering, Suez University, Suez 43721, Egypt

\* Correspondence: e.saleh@qu.edu.sa

**Abstract:** We developed a new optical sensor for tracing Hg(II) ions. The detection affinity examines within a concentration range of 0–4.0  $\mu\text{M}$  Hg(II). The sensor film is based on Methyl 2-hydroxy-3-(((2S,2'R,3a'S,5R)-2-isopropyl-5,5'-dimethyl-4'-oxotetrahydro-2'H-spiro[cy-clohexane-1,6'-im-idazo[1,5-b]isoxazol]-2'-yl)methyl)-5-methylbenzoate (IXZD). The novel synthesized compound could be utilized as an optical turn-on chemosensor for pH. The emission intensity is highly enhanced for the deprotonated form concerning the protonated form. IXZD probe has a characteristic fluorescence peak at 481 nm under excitation of 351 nm with large Stokes shift of approximately 130 nm. In addition, the binding process of IXZD:Hg(II) presents a 1:1 molar ratio which is proved by the large quench of the 481 nm emission peak of IXZD and the growth of a new emission peak at 399 nm (blue shift). The binding configurations with one Hg(II) cation and its electronic characteristics were investigated by applying the Density Functional Theory (DFT) and the time-dependent DFT (TDDFT) calculations. Density functional theory (DFT) and the time-dependent DFT (TDDFT) theoretical results were provided to examine Hg(II)-IXZD structures and their electronic properties in solution. The developed chemical sensor was offered based on the intramolecular charge transfer (ICT) mechanism. The sensor film has a significantly low limit of detection (LOD) for Hg(II) of 0.025  $\mu\text{M}$  in pH 7.4, with a relative standard deviation  $\text{RSD}_r$  (1%,  $n = 3$ ). Lastly, the IXZD shows effective binding affinity to mercury ions, and the binding constant  $K_b$  was estimated to be  $5.80 \times 10^5 \text{ M}^{-1}$ . Hence, this developed optical sensor film has a significant efficiency for tracing mercury ions based on IXZD molecule-doped sensor film.

**Keywords:** optical sensor; pH; Hg(II); ESIPT; ratiometric; DFT



**Citation:** Ali, R.; Ghannay, S.; Messaoudi, S.; Alminderej, F.M.; Aouadi, K.; Saleh, S.M. A Reversible Optical Sensor Film for Mercury Ions Discrimination Based on Isoxazolidine Derivative and Exhibiting pH Sensing. *Biosensors* **2022**, *12*, 1028. <https://doi.org/10.3390/bios12111028>

Received: 28 October 2022

Accepted: 12 November 2022

Published: 16 November 2022

**Publisher's Note:** MDPI stays neutral with regard to jurisdictional claims in published maps and institutional affiliations.



**Copyright:** © 2022 by the authors. Licensee MDPI, Basel, Switzerland. This article is an open access article distributed under the terms and conditions of the Creative Commons Attribution (CC BY) license (<https://creativecommons.org/licenses/by/4.0/>).

## 1. Introduction

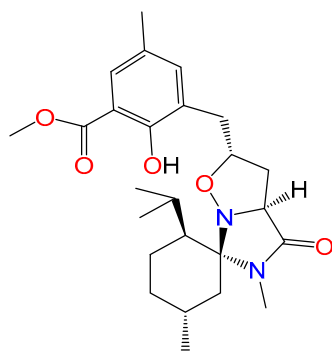
Heavy metal contamination of water resources poses a significant danger to human health and the surrounding environment and causes many associated risks. Despite the efforts to overcome this problem, the industrial boom and multiple human activities led to a steady increase in pollution caused by heavy metals in various water resources. Thus, many global scientific organizations set limits for different concentrations of heavy metal ions. Therefore, many efforts are being introduced to detect the concentrations of various heavy metal ions, involving lead, mercury, arsenic, nickel, and cadmium, to mask the severe health influences of bio-accumulation and bio-magnification [1–5].

Mercury is one of the dangerous heavy metal ions, considered the most toxic element because of its great danger to health, including heart muscle diseases, kidney toxicity,

neurotoxicity, tendency to produce cancer, autoimmune diseases, and male reproductive toxicity [6–10]. Additionally, the surrounding environment is affected by the toxicity of mercury, which results mainly from the handling of many different chemicals and from the other processes that take part in the marine and aquatic environments and the conversion of mercury into various organic and inorganic forms. By auditing, microorganisms can convert inorganic mercury into methylmercury, a conceivable neurolysin [11–13]. Thus, detecting mercury in the environment takes much of people's attention. Memorably, many methods have been used to detect mercury ions such as inductive coupling plasma mass spectrometry, surface-enhanced Raman spectroscopy, and atomic absorption spectrometry, which are expensive and require extended time pretreatment. People with special training have to carry out these processes [14–16]. Chemical sensors display great efficiency in detecting mercury ions due to their biocompatibility, portability, and promise for use in field treatments [17–22].

Researchers developed and designed several significant optical sensors with extreme selectivity and sensitivity to determine several metal ions. Detection of heavy metal ions has been considered one of the essential remarkable and vital research streams in analytical chemistry. The benefits of the fluorescence technique for sensing involve crucial factors. First, molecular fluorescence is enormously sensitive; these measurements produce slight or no destruction to the host structure, thus delivering the capability for wholly non-intrusive sensing. Second, the information provided by the fluorescence techniques shows the system design and environmental behavior of molecules and the way in which these vary in reaction to analyte alterations in the surrounding environments. For example, some heavy metal-sensitive probes labeled to proteins can be quenched or enhanced as the adaptation variations reveal the dye to heavy metals. The biomolecule distribution in a particular environment and under such conditions can be investigated using fluorescence resonance energy transfer (FRET) [23,24]. In addition, the synthesis of isoxazolidines has become increasingly important because of their diverse biological activities [25–27]. Recently, we have described the synthesis of isoxazolidine derivatives which can be used as potential alternatives to modulating T2DM (type 2 diabetes mellitus) [28]. In addition, isoxazolidine is a precursor of many bioactive molecules such as amino acids [29],  $\beta$ -lactams [30], amino lactones [31], and alkaloids accessible by breaking the N-O bond of the isoxazolidine ring [32].

In this project, we developed a novel chemosensor utilizing IXZD for detecting Hg(II) ions, and this sensor is designed utilizing a substantial IXZD sensing molecule. The structure of the IXZD molecule is displayed in Scheme 1. Additionally, the novel probe can be used as a turn-on optical sensor for pH sensing as the luminescence is highly increased in the case of the deprotonated form concerning the protonated form. The proposed mechanism can be referred to as metal–ligand binding between IXZD and Hg(II) ions to introduce a metal complex. The explanation of the formed metal complex is based on an intramolecular charge transfer (ICT) [33–35]. The sensing process of mercury ions by IXZD probe was studied utilizing UV–Vis and emission intensities measurements. The new sensor provides considerable sensitivity and selectivity with a precious value of LOD and rapid reversibility for tracing mercury ions.

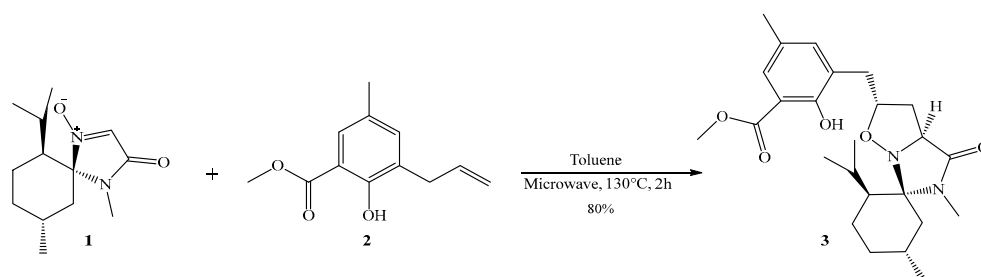


**Scheme 1.** The chemical structure of IXZD molecule.

## 2. Materials and Methods

### 2.1. Chemicals

All the fine chemicals were purchased from Sigma-Aldrich. All chemical solvents were analytical grade and used as received in all experiments. Methyl 2-hydroxy-5-methyl-3-(prop-2-en-1-yl)benzoate (Scheme 2) was purchased from Acros company <https://www.acros.com/> (accessed on 11 November 2022). Stock solutions of the applied metal nitrates were prepared with bi-distilled water before experimentation and directly involved in the experimental series.



**Scheme 2.** Preparation of the sensing probe IXZD.

### 2.2. Instruments

The NMR spectrum of the sensing compound was measured utilizing a JEOL JNMECA 600 spectrometer (600-MHz for  $^1\text{H}$  and 150-MHz for  $^{13}\text{C}$ ) regarding TMS, Tetramethylsilane as an internal standard. Melting points were detected based on a Kofler Microhot Stage Instrument. UV–Vis spectra were attained in a 1 cm quartz cell with an Evolution™\_200-series/UV–Visible spectrophotometer. Fluorometric measurements, including excitation and emission spectra, were measured on a JASCO FP-6300 spectro-fluorometer in a 1 cm quartz cell.

### 2.3. Synthesis of IXZD

In a 10 mL glass vial, nitron 1 (150 mg, mmol) was dissolved with methyl 2-hydroxy-5-methyl-3-(prop-2-en-1-yl) benzoate 2 in 6 mL of toluene [23]. The reaction has been activated by a mono-wave 200 system operating at 130 °C for 2 h. The obtained product has been purified by flash chromatography on silica gel (EtOAc/PE 2/8) to provide the cycloadduct 3, as shown in the following Scheme 2. The NMR spectrum is exhibited in Figure S1 (Supplementary Materials).

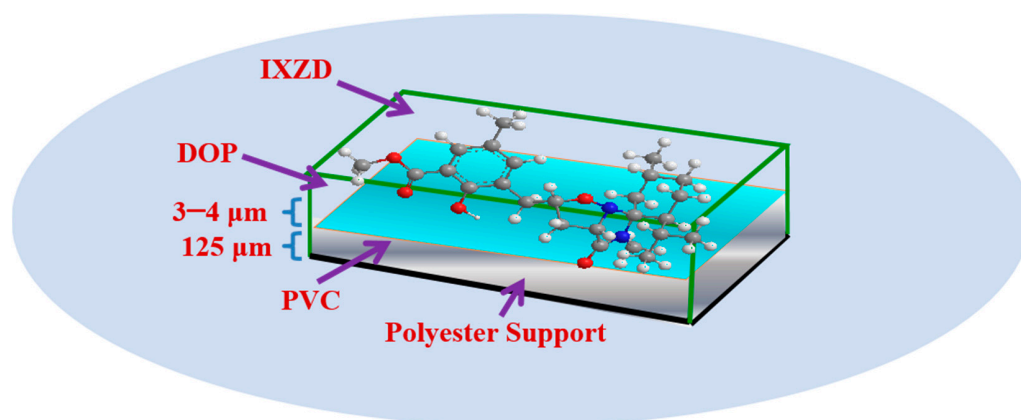
### 2.4. Optical Characteristics of IXZD

The UV–Vis spectra of  $2 \times 10^{-3}$  M IXZD were collected in 20 mM Britton–Robinson (BR) buffer, BR is a “universal” buffer for pH 2–12, and it consists of boric acid, phosphoric acid, and acetic acid that has been titrated to the desired pH with sodium hydroxide. Through titration, we fixed the total volume of the prepared solution of IXZD to 2.0 mL. The luminescence intensities of the prepared solutions were measured at different pH values utilizing the same conditions. The excitation and emission slit widths for all investigated solutions were 5 nm. A definite concentration of IXZD in an aqueous BR buffer (20 mM) was used for the luminescence titration to demonstrate the efficiency of the sensor at different pH. Various prepared solutions of BR buffer with a wide range of pH scales from 2 to 12.5 were used to investigate the pH sensing of the chemical sensor.

### 2.5. Design of the Optical Film

The sensing film was designed by introducing a cocktail solution. This solution consists of 2.0 mg IXZD, 25.4 mg of Polyvinyl chloride, and 51 mg of dioctyl phthalate plasticizer in 1.8 mL THF (Tetrahydrofuran). Moreover, the cocktail solution was mixed for 6 h. A knife coater spread the solution on a polyester polymer support [36]. The sensor film

was left to dry in the air for 2 h. The estimated thickness of the sensor film was calculated from the cocktail quantity to be 3–4  $\mu\text{m}$  after evaporation of the solvent, as exhibited in Scheme 3.



**Scheme 3.** Schematic diagram of IXZD sensor film.

### 2.6. The Binding Study

The stoichiometric of the IXZD sensing probe and Hg(II) interaction was investigated by applying Job's method [37,38]. The chemical binding was exploited in pH 7.4 buffer solution using a molar ratio of 1:1 of  $1 \times 10^{-6}$  M IXZD sensing compound and Hg(II) ions. The relation between the molar ratios of the reactants (9:1 to 1:9) against the luminescence intensities ratio of the IXZD probe at (399/481) was studied.

## 3. Results

### 3.1. The Optical Properties of IXZD

The optical measurements of the IXZD sensing probe were collected in DMSO: MeOH (5:95)-based BR buffer (20 mM) at physiological pH (7.4). The IXZD probe showed considerable properties, including a significant Stokes shift  $\approx 130$  nm as shown in Figure 1a. IXZD shows characteristic absorption peaks at 242 and 320 nm. Moreover, it displays a prominent fluorescence peak at 481 nm under excitation with 351 nm. ESIPT (Excited state intramolecular proton transfer) chromophores absorb photons in the UV region and emit energy in the visible region. The absorption and emission wavelengths are based predominantly on the molecular structure of the studied probes and their attached functional, active groups. Additionally, the absorption and emission maxima of the IXZD probe are independent of the concentration. This work uses the IXZD absorption spectra to demonstrate its efficiency as a pH chemical probe. The absorption spectra of IXZD were carried out at various pH values using 20 mM BR buffer solutions. Figure 1b exhibits the absorption spectra of IXZD; it shows two distinct peaks at 242 nm and 320 nm, which are assigned to the  $\pi-\pi^*$  and  $n-\pi^*$  transitions.

With the rising pH values of the studied solution containing 0.5 mg/mL IXZD, a continuing enhancement in the absorption maximum of the peak located at 320 nm is perceived, associated with the development of an additional intense absorption peak located at 352 nm with a distinctive isosbestic point at approximately 326 nm. The ESIPT mechanism is responsible for the red shift of the absorption band, and the absorbance increment of the new peak is due to the ICT mechanism of the phenoxide tautomer in the deprotonated IXZD anion structure that takes place in the ground state. Figure 2 exhibits the relation of the IXZD absorbance against the pH change of the investigated solution. Additionally, the inset of Figure 2 displays the calibration plot attained for the absorbance wavelengths at 320 nm and 352 nm of the IXZD probe versus the pH values of the studied solutions in the presence of 20 mM BR buffer. The harmonic relationship is established during the pH-titrimetric reaction, where the absorbance peak at 320 nm gradually shifts, and the second absorbance peak at 352 nm is synchronously enhanced.



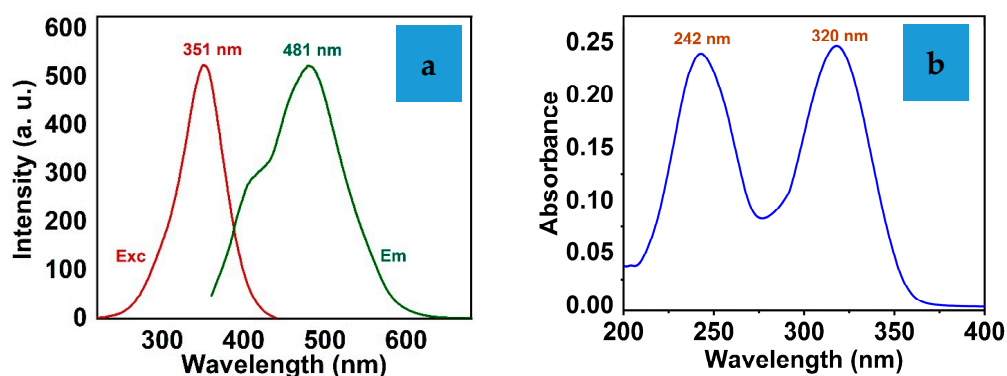


**Figure 1.** IXZD Optical Properties. (a) Fluorescence/excitation spectra under 351 nm excitation and (b) UV-Vis spectrum.

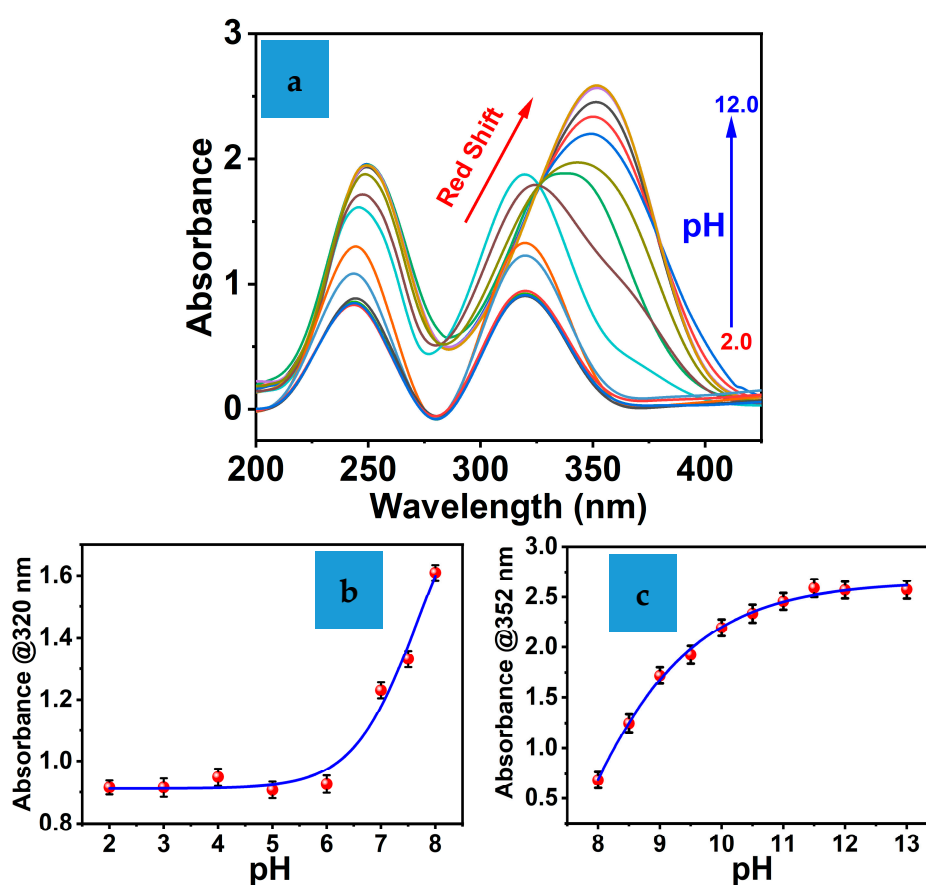


**Figure 2.** (a) Absorbance spectra of IXZD at various pH values; (b,c) the absorbance of the IXZD versus pH.

Figure 3 represents the influence of the pH on the luminescence intensities of IXZD. IXZD exhibits a weak emission peak centered at 441 nm in acidic pH. The emission maximum at 441 nm enhances and changes to 481 nm, red shift, by increasing the pH to six as shown in Figure 3a. This can be attributed to the ICT mechanism of the phenoxide tautomer in the deprotonated IXZD anion structure that occupies the ground state. By transferring the pH from the acidic medium to the basic medium, pH = 6–12, the enhancement of the emission intensities at 481 nm takes place (see Figure 3b). The inset graphs introduce the relation of IXZD fluorescence intensities at 481 nm against the pH of the studied solutions.

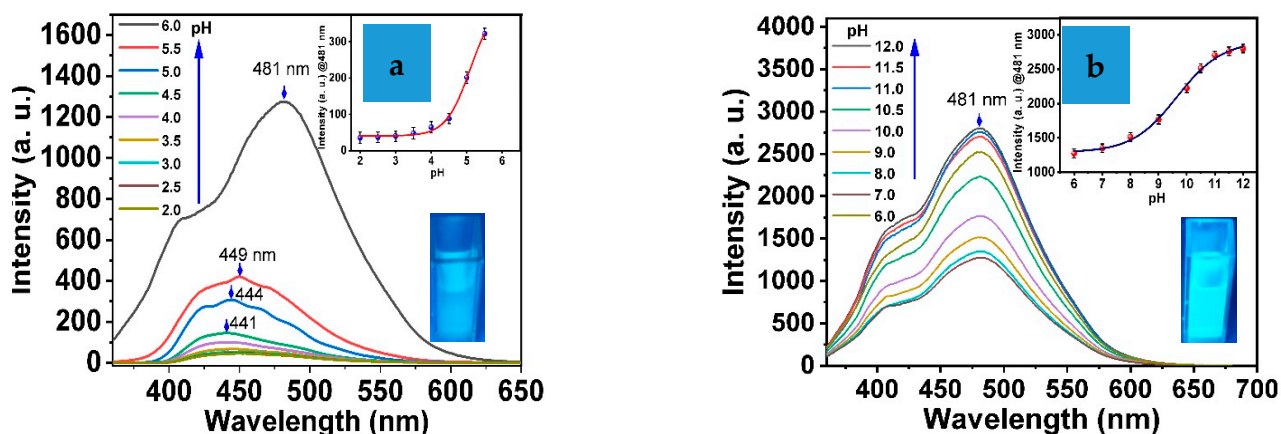


**Figure 3.** Emission spectra of IXZD at various pH values: (a) pH range (2–6); (b) pH range (6–12).

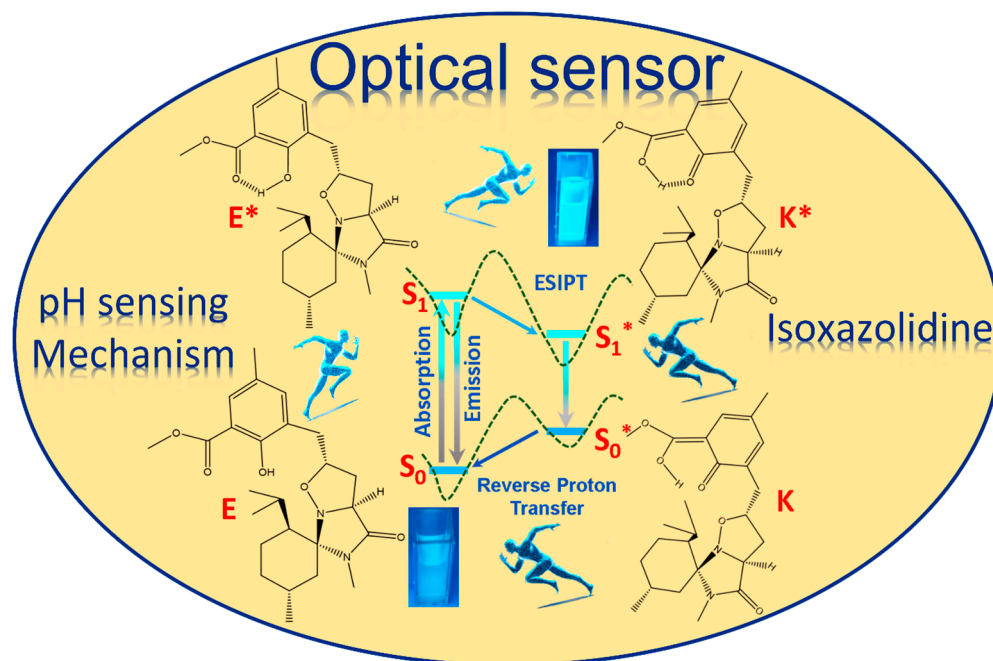
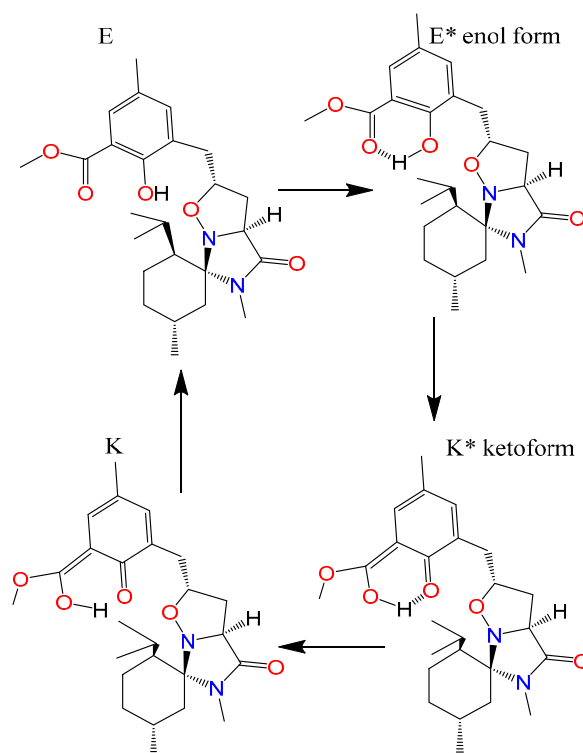
### 3.2. Study the pH Property of the Chemical Probe

In the present work, we introduce a novel type of pH sensor. The mechanism of the new chromophore involves the ESIPT mechanism. Additionally, the basic idea of the ESIPT mechanism depends on the excitation of the organic probe. A photoinduced proton tautomerization can introduce this from the enol form ( $E^*$ ) to the phototautomer keto form ( $K^*$ ) with the intramolecular hydrogen bond. This is induced by internal proton transfer from a hydroxyl group in the enol form to the oxygen atom that acts as a highly electronegative withdrawn atom. When the keto form relaxes into the ground state, the inverse proton transfer mechanism returns the desired enol structure. ESIPT luminescence mechanism delivers distinctive characteristics, including strong luminescence and a significant Stokes shift value, due to the fluorescence produced from  $K^*$ . The mainly unique feature of IXZD is its luminescence performance. This chemical label is present in the enol tautomer structure in the ground state. During the excitation process, in the presence of a photon, a proton is moved from the hydroxyl donor functional group to the carbonyl acceptor group, which generates the excited state proton transfer tautomer. The constructed excited state then consumes its energy through the relaxation process to the lower energy ground state, escorted by luminescence. Remarkably, the energy level of the keto structure tautomer  $K^*$  in the excited state, which presents based on the proton transfer, has less energy level than the enol structure tautomer  $E^*$ . Additionally, the keto structure tautomer  $K$  in the ground state has a greater energy level than the enol structure tautomer  $E$ .

As a result, the energy transfer from excited  $K^*$  state to the ground  $k$  state is less than the energy released during the transformation from the excited  $E^*$  state to the ground  $E$  state. Thus, the Stokes shift of the ESIPT IXZD chemical probe in keto form is more significant than that of the enol form (as shown in Scheme 4). Furthermore, Scheme 4 shows two sets of energy levels:  $S_0$  and  $S_0^*$ , which represent enol and keto tautomers that present at the ground states, and  $S_1$  and  $S_1^*$ , which represent the enol and keto tautomers that provide the first singlet excited states separately [34]. The asterisk denotes the tautomer that formed during proton transfer. The hypothesized enol tautomer processes show rapid enol tautomer structure relaxation from the excited to the ground state, accompanied by decreasing emission or a faster energy route involving hydrogen proton transfer from the enol form to the keto tautomer structures.

In the most common design of pH sensor, pH probes rely on weak acidic dyes whose dissociated and undissociated forms have different absorption or fluorescence in the pH range of interest. Although a great variety of pH indicators is known, only a few possess the requirements for use in a pH probe [39], including (a) a pK in the pH range of interest; (b) strong absorption within UV–Vis range, making them compatible with the excitation light sources; (c) photostability and chemical stability; (d) lack of toxicity especially when the probe embedded in a polymer film, and (e) the availability of functional groups suitable

for chemical immobilization. In the case of fluorescence-based pH probes, large Stokes' shifts and lack of quenchability by oxygen and other sample constituents are desirable.



**Scheme 4.** The ESIPt mechanism of IXZD.

### 3.3. Sensor Characteristics

The colorimetric and luminescence titration techniques were used to evaluate the IXZD molecule sensing capacity towards the mercury ions. The absorbance peak at 320 nm regularly decreased in the presence of Hg(II) ions. At the same time, the absorbance peak at 242 nm was enhanced. The ratiometric absorbances of the IXZD chemical probe in the

presence of Hg(II) were noticed between these two significant peaks, with a considerable isobestic point located at 292 nm, as shown in Figure 4a. Additionally, a significant curve-fit relation was introduced concerning the IXZD absorbance values ratio at 242 and 320 nm and the amount of Hg(II) ions between 0 and 1.5  $\mu\text{M}$  (see Figure 4b).

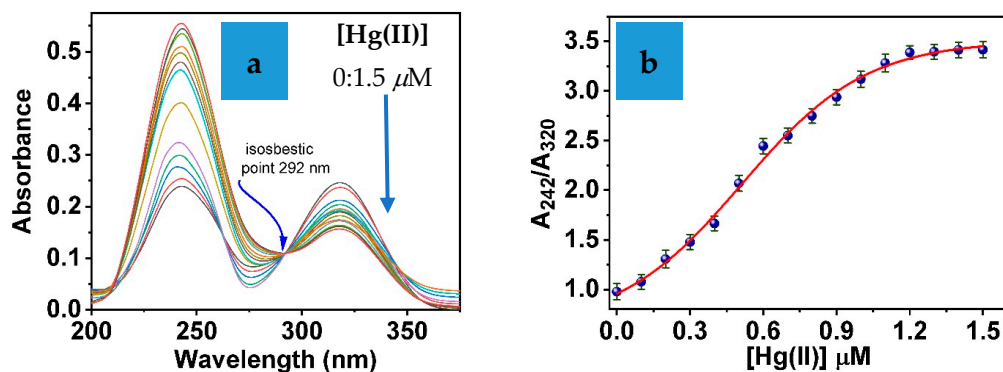


Figure 4. (a) Behavior of UV-Vis spectrum of IXZD in the presence of 0:1.5  $\mu\text{M}$  Hg(II) and (b)  $A_{242}/A_{320}$  absorbance ratio of IXZD against [Hg(II)].

Furthermore, the  $A_{242}/A_{320}$  absorbances ratio of the IXZD is directly proportional to the concentration of Hg(II) ions up to a 1:1 molar ratio of ligand/metal. Compared to the UV-Vis spectrum of free IXZD, the quenching of the absorbance peak at 320 nm and the enhancement of the absorbance peak at 242 nm, respectively, prove the strong attendance of IXZD for the binding process-based IXZD-Hg(II) chelation. The disparities in the UV-Vis spectrum can be revealed by the significant IXZD chelated with Hg(II) because of the behavior of the conjugated electronic structure [40].

The fluorescence titration of the IXZD sensing molecule versus Hg(II) concentrations was carried out in a 20 mM BR buffer solution at a pH of 7.4. The IXZD molecules exhibit a central emission peak at 481 nm under 351 nm excitation wavelength (Figure 5a). The binding of Hg(II) to the IXZD with a molar ratio of 0:1 sensing probe to Hg(II) ions immediately decreased the luminescence of the maximum peak IXZD at 481 nm with the growth of a new emission maximum 399 nm, indicating IXZD chelates mercury ions. The emission maximum at 481 nm was significantly decreased by introducing Hg(II) metal ions into the system, proposing additional proof of the chelation of Hg(II) ions by the IXZD sensing molecule. The IXZD emission did not change or exhibit any changes in the emission peaks on consistent addition of mercury ions  $\approx 12 \mu\text{M}$  (inset Figure 5), confirming the binding process of Hg(II)-IXZD with an equivalent ratio of 1:1 (metal: IXZD sensing probe).

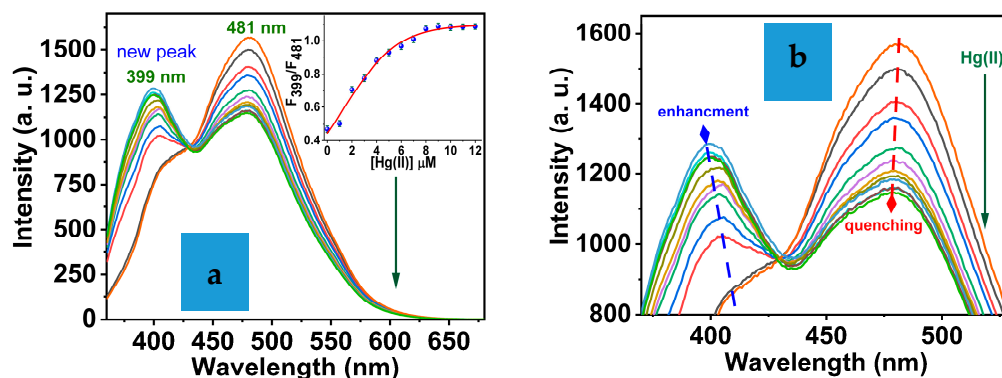
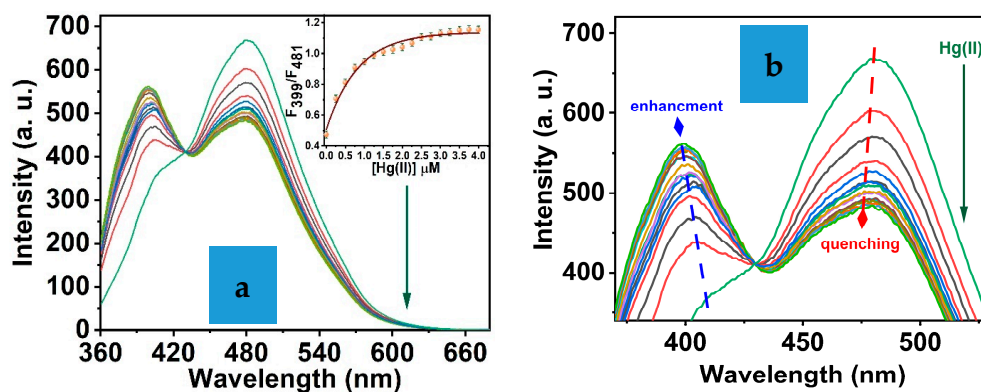


Figure 5. (a) Fluorescence titration of Hg(II)-IXZD with a molar ratio of 0:1 (metal: IXZD); inset figure represents the IXZD emission intensities ratio at 399 and 481 nm versus [Hg(II)]; (b) IXZD emission intensities scope at 399 nm and 481 nm, respectively.

### 3.4. The Sensing Film

The response of sensor film towards Hg(II) was investigated. The fluorescence spectra of the sensor film in the presence of various [Hg(II)] were detected, as shown in Figure 6a. During the fluorescence titration, a significant increment in the fluorescence peak at 399 nm was noticed. The quenching of the emission central peak at 481 nm confirmed the chelation of mercury ions by the IXZD sensing probe. Further, the emission peak at 475 nm was significantly enhanced by gradually increasing [Hg(II)], and inset Figure 6a exhibits the dependence of the  $F_{399}/F_{481}$  ratio versus [Hg(II)] that proved the complex formation. The reaction mechanism can be referred to as the internal charge transfer (ICT) mechanism [41]: IXZD acts as a donor molecule that chelates Hg(II) metal ions which act as a receptor. The IXZD sensor exhibited a high affinity to mercury with a 0 to 4  $\mu\text{M}$  concentration range. The LOD was estimated from the fluorescence titration of IXZD versus Hg(II). Assuming that emission intensity can be identified with a precision of  $\pm 1\%$ , the LOD is estimated to be 0.025  $\mu\text{M}$  Hg(II) [42,43]. Therefore, the IXZD sensor significantly influences the chemical sensor for tracing mercury ions.



**Figure 6.** (a) Fluorescence titration of the sensor film; inset figure represents the IXZD emission intensities ratio at 399 and 481 nm versus [Hg(II)]; (b) IXZD emission intensities scope at 399 nm and 481 nm, respectively.

### 3.5. Sensitivity and Selectivity of IXZD

The influence of different metal ions such as alkali, alkaline, and transition metal ions on the sensitivity of IXZD was studied. The interference experiments were carried out, the IXZD chemosensor fluorescence intensities were recorded, and the investigated interfering ions were added to the surrounding medium during the sensing procedure. The sensing efficacy of the optical sensor film to Hg(II) ions does not show any alterations due to the presence of other metal ions. Therefore, the attendance of the different cations to affect the binding model of Hg(II)-IXZD was examined in a 20 mM BR buffer medium using fluorescence intensity detections (Figure 7a). The interfering cations did not significantly interfere with the sensing mechanism of the chemosensor film-IXZD to mercury ions. Thus, the chemosensor film shows considerable sensitivity for tracing Hg(II).

The binding stoichiometric of the IXZD-Hg(II) chelation reaction was estimated using Job's plot [44] based on the fluorescence intensities of IXZD as presented in Figure 7b. Job's scheme was designed by varying the concentration of mercury ions (0:1 mole fraction) versus the fluorescence intensities ratio of IXZD sensing molecules. During the addition process of Hg(II), the emissions of the IXZD peaks at 399 and 481 nm were recorded. A 2.0 mL mixture with Hg(II) ions and IXZD chemical sensor with a molar ratio of (1:1) was applied in a buffered medium with a pH of 7.4 utilizing (20 mM BR solution). The resulting mixture has a 10  $\mu\text{M}$  Hg(II)-IXZD. The emission ratio of 481/399 against the concentration Hg(II) exhibits the fluorescence IXZD emission taking place at 0.5 equivalent, providing that the stoichiometric of Hg(II): IXZD ratio is 1:1. The resulting data agree with the absorbance results.



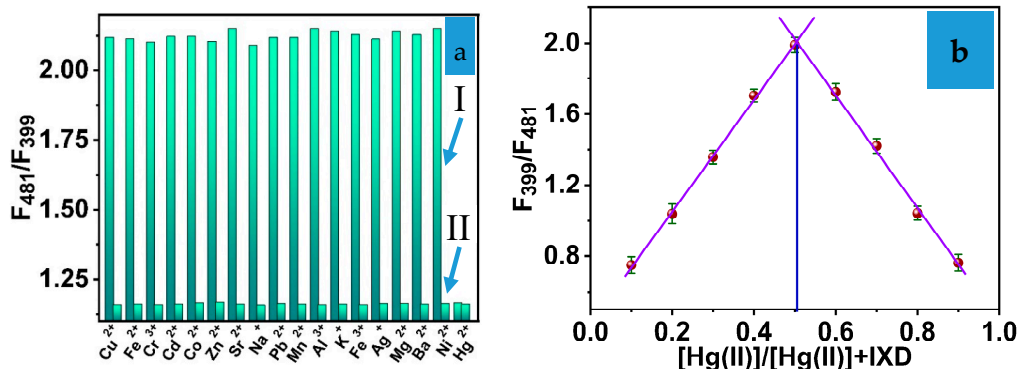


**Figure 7.** (a) IXZD emission spectra at 481 nm under 351 nm excitation (I) in the presence of interfering cations and (II) interfering cations and Hg(II). The IXZD: Hg(II) is 1:1; (b) Job’s plot for determination of the IXZD: Hg(II) stoichiometry.

### 3.6. Binding Reaction

The Benesi–Hildebrand equation was applied to investigate the binding reactivity of the IXZD sensing molecule to mercury ions. The binding constant of IXZD-Hg(II), depending on the fluorescence intensities data, was calculated:

$$\frac{1}{F - F_0} = \frac{1}{K_b (F_{max} - F_0) [Hg(II)]} + \frac{1}{F_{max} - F_{min}}$$

$F_0$ ,  $F$ , and  $F_{max}$  are emission intensities of the IXZD at 399 nm detected in the absence of Hg(II) at various concentrations and a 1:1 equivalent molar ratio (IXZD: mercury ions), respectively, and where  $K_b$  is the binding constant. The Benesi–Hildebrand equation estimates the  $K_b$  to be  $5.8 \times 10^5 \text{ M}^{-1}$  (Figure 8a) [44].

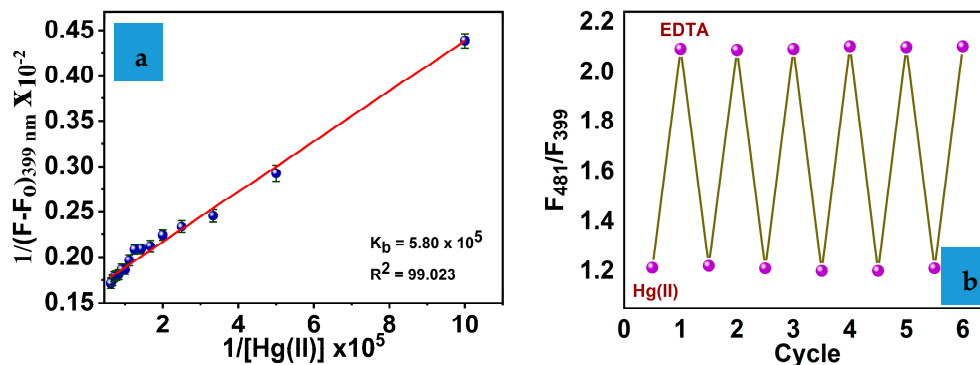


**Figure 8.** (a) Benesi–Hildebrand formulation based on  $1/(F-F_0)$  versus Hg(II) (b) The reversibility of IXZD optical sensor using EDTA at  $\lambda_{em} = 481 \text{ nm}$ .

Moreover, the recycling of the sensing affinity based on the binding of the IXZD-Hg(II) complex was investigated by the titration of the IXZD film versus ethylenediaminetetraacetic acid (EDTA) in the presence of Hg(II) [45–47]. Introducing EDTA to the surrounding medium with the sensor film after adding the Hg(II) ions increases the emission peak at 399 nm and subsequently decreases the 481 nm peak. This behavior can be attributed to the binding interaction of Hg(II) by EDTA, as shown in Figure 8b. This substitution reaction was confirmed by activating the free IXZD sensing molecule in the sensor film and enhancing the emission of 399 nm under 351 nm excitation. Thus, the IXZD optical film can be a characteristic sensor for tracing Hg(II) cations.

Table 1 summarizes the LOD values of the optical sensor-based organic molecules used in Hg(II) detection. The present work exhibits a great efficiency for detection of Hg(II) ions with respect to recent research-based organic molecules.

**Table 1.** Comparison of the IXZD sensor with recently research-based Hg(II) detection.

Sensor	LOD (M)	References
Rhodamine B	$1.34 \times 10^{-6}$	[48]
Rhodamine B + Polymer	$0.05 \times 10^{-6}$	[49]
BODIPY	$0.77 \times 10^{-6}$	[50]
Thiourea	$0.1 \times 10^{-6}$	[51]
Crown-ether	$0.1 \times 10^{-6}$	[52]
Coumarine	$0.29 \times 10^{-6}$	[53]
Pyrene	$1.74 \times 10^{-6}$	[54]
Anthracene	$3.2 \times 10^{-6}$	[55]
Oxadiazole	$1.5 \times 10^{-6}$	[56]
IXZD molecule	$0.025 \times 10^{-6}$	Present work

### 3.7. Theoretical Calculations

Density functional theory (DFT) and the time-dependent DFT (TDDFT) theoretical calculations were performed using the Gaussian09 program [57] to understand the electronic properties of the ligand alone, the ligand in the presence of the  $\text{H}_3\text{O}^+$  molecule, and the ligand forming a complex with  $\text{Hg}^{2+}$ . These electronic properties contribute to ESIPT properties [58] and the quenching of ESIPT fluorescence. The PBE1PBE functional and 6-31G(d)/Lanl2dz basis sets were applied to optimize the different structures. Hg atoms were treated by LANL2DZ basis set, and all other atoms were treated by 6-31G(d). The solvation model SMD and water were included in all the calculations. We performed vibrational frequency calculations at the same theory level to confirm the complex stability with the IXZD chemical probe.

Using the optimized structures, we have applied TDDFT calculations with solvation model SMD and water through the PBE1PBE/ aug-cc-pVDZPP/6-31+G(d) level of theory. Dunning's double zeta augmented correlation consistent polarized basis set (aug-cc-pVDZPP) was used for Hg along with the corresponding effective core potentials (ECP) [59,60]. The optimized structures with solvation model SMD and water of the ligand alone (IXZD), the ligand in the presence of the  $\text{H}_3\text{O}^+$  molecule ( $\text{H}_3\text{O}^+$ -IXZD), and the  $\text{Hg}^{2+}$  complexes ( $\text{Hg}^{2+}$ -IXZD) are represented in Figure 9. The relative energies for the different  $\text{Hg}^{2+}$  complexes are given in Table 2.

**Table 2.** Values of relative energies of the  $\text{Hg}^{2+}$  Complexes with solvation model SMD and water.

Complex	Relative Energy (kcal/mol)
$\text{Hg}^{2+}$ -IXZD	0
$\text{Hg}^{2+}$ -IXZD'	1.8
$\text{Hg}^{2+}$ -IXZD''	8.2

We show in Figure 9 that  $\text{Hg}^{2+}$  can have short interactions with three oxygens and one nitrogen of the ligand, as in  $\text{Hg}^{2+}$ -IXZD. We propose that this structure is the reference as it has the lowest energy among the other conformations. In  $\text{Hg}^{2+}$ -IXZD', the Hg has two short interactions with one nitrogen and one oxygen belonging to the ring of the ligand and two long interactions with two oxygens. The relative energy for this compound is  $1.8 \text{ kcal mol}^{-1}$ . In  $\text{Hg}^{2+}$ -IXZD'', we have only two long interactions with two oxygens of the ligand. The relative energy for this last compound is  $8.2 \text{ kcal mol}^{-1}$ .

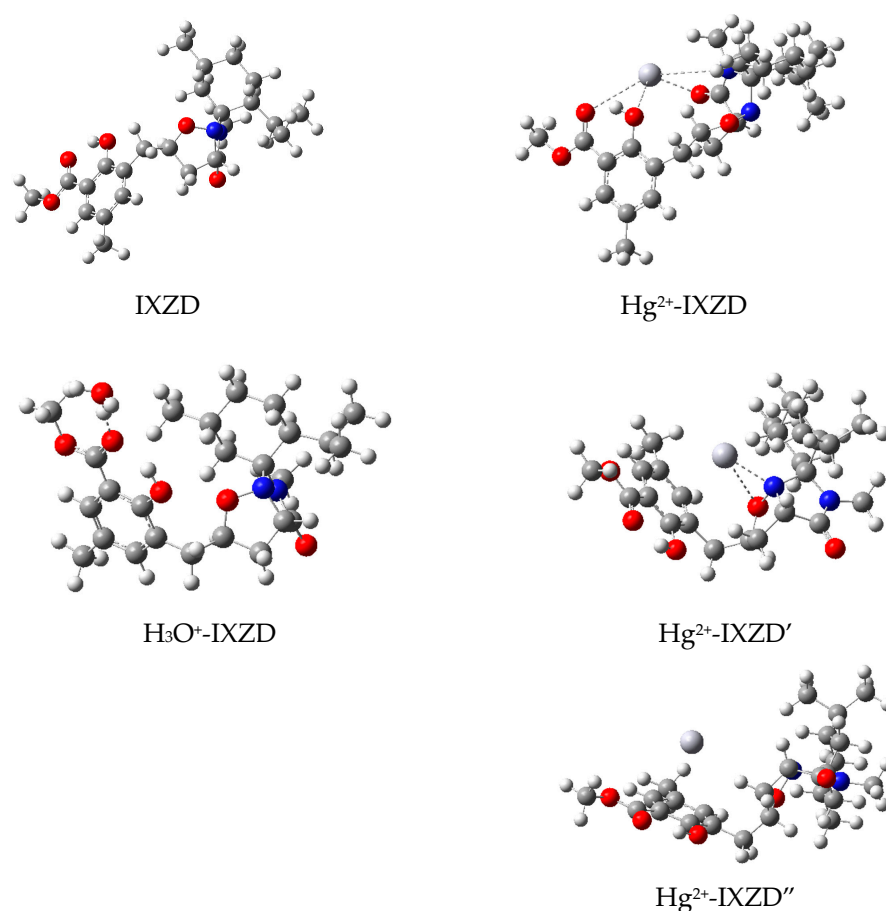


**Figure 9.** Complexes L,  $\text{H}_3\text{O}^+$ -L, and  $\text{Hg}^{2+}$ -L models optimized by DFT with solvation model SMD and water.

The possible transitions were calculated for the most stable structures by performing time-dependent DFT. The selected molecular orbitals of IXZD,  $\text{H}_3\text{O}^+$ -IXZD, and  $\text{Hg}^{2+}$ -IXZD are presented in Figure 10. TDDFT data involving electronic transitions, wavelength, and oscillator strength are found in Table 3. The electron density in the L molecule is mainly detected on the aromatic ring. For the charge redistribution about the hydrogen-bonded parts, the hydroxyl moiety contributes largely to HOMO, while its contribution decreases in LUMO. It indicates that the electron density shifts from the hydroxyl group to the adjacent oxygen upon photoexcitation of IXZD from state  $S_0$  to state  $S_1$ , which provides the tendency for ESIPT reaction [46].

**Table 3.** TDDFT data of selected electronic transitions, absorption energies, and oscillator strengths.

Complex	Transition	$\lambda(\text{nm})$	Oscillator Strength
IXZD	HOMO $\rightarrow$ LUMO	303	0.1584
$\text{H}_3\text{O}^+$ -IXZD	HOMO $\rightarrow$ LUMO	318	0.1338
$\text{Hg}^{2+}$ -IXZD	HOMO $\rightarrow$ LUMO	599	0.0404

In  $\text{H}_3\text{O}^+$ -IXZD, we see a similar effect in the electronic transition in IXZD. The HOMO is now more delocalized on the whole molecule. This results in a lower value of the oscillator strength for this transition (0.133 for  $\text{H}_3\text{O}^+$ -IXZD compared to 0.158 for IXZD), showing less electron density transfer from the hydroxyl group to the adjacent oxygen. This results in less tendency for ESIPT reaction and contributes to the quenching of the ESIPT-based fluorescence probe. This suggests that this effect is enhanced in the presence of more  $\text{H}_3\text{O}^+$  molecules when the medium is more acidic. In  $\text{Hg}^{2+}$ -IXZD, the transition from

HOMO to LUMO offers an intramolecular charge transfer (ICT): the electron density in the HOMO is mainly on the hydroxyl group and the aromatic ring of the ligand IXZD, but the electron density in the LUMO is essentially distributed on the metal Hg. There is no shift of the electron density from the hydroxyl group to the adjacent oxygen, which blocks the tendency for ESIPT reaction. Thus, the ICT from the IXZD molecule to Hg(II) contributes to the quenching of the ESIPT-based fluorescence probe. These results are supported by the low value of the oscillator strength (Table 3).

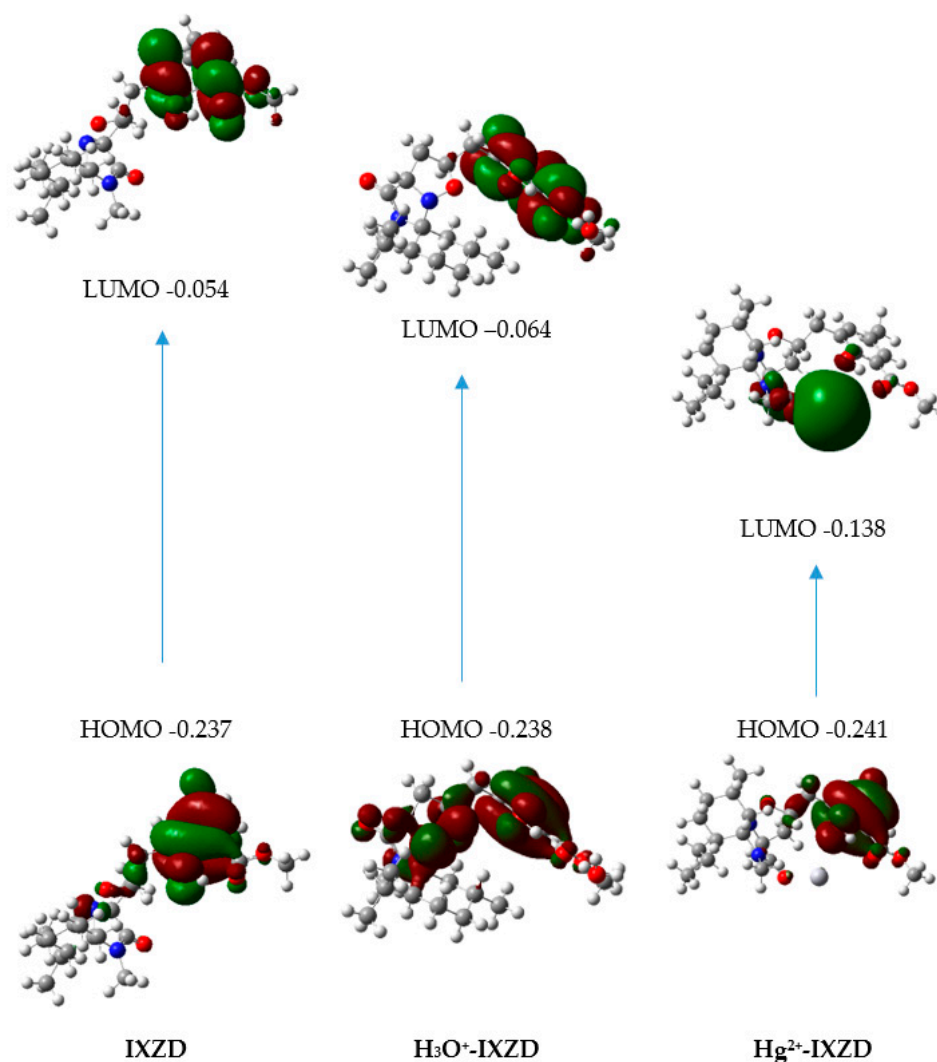


Figure 10. Frontier orbitals and their energies for L, H<sub>3</sub>O<sup>+</sup>-IXZD, and Hg<sup>2+</sup>-IXZD.

#### 4. Conclusions

The IXZD sensing molecule was designed and developed as an enormously selective chemosensor for tracing Hg(II). The properties of the IXZD molecule are based on UV–Vis absorbance spectra, and fluorescence spectra were examined in the presence of mercury ions using a 20 mM BR buffer system at an adjusted pH medium. The IXZD molecule was embedded in a PVC film. The fabricated sensing film exhibits excellent selectivity and sensitivity to mercury ions. The detection limit was determined to be 0.025 mM Hg(II) concentration without showing any interference with the presence of any cations in the surrounding medium. Additionally, Hg(II) ions affect the IXZD solution rapidly, decreasing the fluorescence peak at 481 nm and enhancing the fluorescence of a new fluorescence peak at 399 nm. Herein, we utilized Job's plot to investigate that IXZD binds to Hg(II) ions with a ratio of 1:1. The proposed mechanism of sensing molecule is based on the binding of Hg(II)

by IXZD molecule in the solution vicinity and producing an IXZD-Hg(II) complex. Density functional theory (DFT) and the time-dependent DFT (TDDFT) theoretical calculations were provided to study the Hg(II) complexation structures and their electronic properties in solution. The formation constant of the formed complex was calculated using the Benesi–Hildebrand equation. Lastly, the synthesized IXZD chemosensor could be used efficiently to detect Hg(II) ions.

**Supplementary Materials:** The following supporting information can be downloaded at: <https://www.mdpi.com/article/10.3390/bios12111028/s1>, Figure S1: <sup>1</sup>H spectrum of the synthesized compound. Figure S2: <sup>13</sup>C spectrum of the synthesized compound.

**Author Contributions:** Conceptualization, S.M.S. and R.A.; methodology, S.M.S. and R.A.; software, R.A. and S.G.; validation, S.M.S., R.A. and K.A.; formal analysis, K.A. and F.M.A.; investigation, F.M.A.; resources, S.M.S. and R.A.; data curation, S.M.S. and R.A.; writing—original draft preparation, S.M.S., R.A. and S.M.; writing—review and editing, S.M.S. and R.A.; visualization, S.G. and K.A.; supervision, S.M.S. and R.A.; project administration, S.M.S. and R.A.; funding acquisition, S.M.S. All authors have read and agreed to the published version of the manuscript.

**Funding:** The authors extend their appreciation to the Deputyship for Research and Innovation, Ministry of Education, Saudi Arabia for funding this research work through the project number (QU-IF-4-3-2-29870). The authors also thank to Qassim University for technical support.

**Institutional Review Board Statement:** Not applicable.

**Informed Consent Statement:** Not applicable.

**Data Availability Statement:** Not applicable.

**Conflicts of Interest:** The authors declare no conflict of interest.

## References

1. Zamora-Ledezma, C.; Negrete-Bolagay, D.; Figueroa, F.; Zamora-Ledezma, E.; Ni, M.; Alexis, F.; Guerrero, V.H. Heavy metal water pollution: A fresh look about hazards, novel and conventional remediation methods. *Environ. Technol. Innov.* **2021**, *22*, 101504. [[CrossRef](#)]
2. Junaid, M.; Hashmi, M.Z.; Malik, R.N.; Pei, D.S. Toxicity and oxidative stress induced by chromium in workers exposed from different occupational settings around the globe: A review. *Environ. Sci. Pollut. Res.* **2016**, *23*, 20151–20167. [[CrossRef](#)] [[PubMed](#)]
3. Rehman, K.; Fatima, F.; Waheed, I.; Akash, M.S.H. Prevalence of exposure of heavy metals and their impact on health consequences. *J. Cell. Biochem.* **2018**, *119*, 157–184. [[CrossRef](#)] [[PubMed](#)]
4. Jaishankar, M.; Tseten, T.; Anbalagan, N.; Mathew, B.B.; Beeregowda, K.N. Toxicity, mechanism and health effects of some heavy metals. *Interdiscip. Toxicol.* **2014**, *7*, 60–72. [[CrossRef](#)]
5. Ali, H.; Khan, E.; Ilahi, I. Environmental Chemistry and Ecotoxicology of Hazardous Heavy Metals: Environmental Persistence, Toxicity, and Bioaccumulation. *J. Chem.* **2019**, *2019*, 6730305. [[CrossRef](#)]
6. Holmes, P.; James, K.; Levy, L. Is low-level environmental mercury exposure of concern to human health? *Sci. Total Environ.* **2009**, *408*, 171–182. [[CrossRef](#)]
7. Ye, B.-J.; Kim, B.-G.; Jeon, M.-J.; Kim, S.-Y.; Kim, H.-C.; Jang, T.-W.; Chae, H.-J.; Choi, W.-J.; Ha, M.-N.; Hong, Y.-S. Evaluation of mercury exposure level, clinical diagnosis and treatment for mercury intoxication. *Ann. Occup. Environ. Med.* **2016**, *28*, 1–8. [[CrossRef](#)]
8. Bernhoft, R.A. Mercury Toxicity and Treatment: A Review of the Literature. *J. Environ. Public Health* **2012**, *2012*, 1–10. [[CrossRef](#)]
9. Genchi, G.; Sinicropi, M.S.; Carocci, A.; Lauria, G.; Catalano, A. Mercury exposure and heart diseases. *Int. J. Environ. Res. Public Health* **2017**, *14*, 74. [[CrossRef](#)]
10. Driscoll, C.T.; Mason, R.P.; Chan, H.M.; Jacob, D.J.; Pirrone, N. Mercury as a Global Pollutant: Sources, Pathways, and Effects. *Environ. Sci. Technol.* **2013**, *47*, 4967–4983. [[CrossRef](#)]
11. Gworek, B.; Bemowska-Kalabun, O.; Kijeńska, M.; Wrzosek-Jakubowska, J. Mercury in marine and oceanic waters—A review. *Water Air Soil Pollut.* **2016**, *227*, 1–19. [[CrossRef](#)] [[PubMed](#)]
12. Regnell, O.; Watras, C.J. Microbial Mercury Methylation in Aquatic Environments: A Critical Review of Published Field and Laboratory Studies. *Environ. Sci. Technol.* **2018**, *53*, 4–19. [[CrossRef](#)]
13. Lee, S.-W.; Lowry, G.V.; Hsu-Kim, H. Biogeochemical transformations of mercury in solid waste landfills and pathways for release. *Environ. Sci. Process. Impacts* **2016**, *18*, 176–189. [[CrossRef](#)]
14. Amde, M.; Yin, Y.; Zhang, D.; Liu, J. Methods and recent advances in speciation analysis of mercury chemical species in environmental samples: A review. *Chem. Speciat. Bioavailab.* **2016**, *28*, 51–65. [[CrossRef](#)]



15. Sarfo, D.K.; Sivanesan, A.; Izake, E.L.; Ayoko, G.A. Rapid detection of mercury contamination in water by surface enhanced Raman spectroscopy. *RSC Adv.* **2017**, *7*, 21567–21575. [[CrossRef](#)]
16. Aragay, G.; Pons, J.; Merkoçi, A. Recent Trends in Macro-, Micro-, and Nanomaterial-Based Tools and Strategies for Heavy-Metal Detection. *Chem. Rev.* **2011**, *111*, 3433–3458. [[CrossRef](#)]
17. Pavase, T.R.; Lin, H.; Hussain, S.; Li, Z.; Ahmed, I.; Lv, L.; Sun, L.; Shah, S.B.H.; Kalhor, M.T. Recent advances of conjugated polymer (CP) nanocomposite-based chemical sensors and their applications in food spoilage detection: A comprehensive review. *Sens. Actuators B Chem.* **2018**, *273*, 1113–1138. [[CrossRef](#)]
18. Dang, Q.-Q.; Wan, H.-J.; Zhang, X.-M. Carbazolic Porous Framework with Tetrahedral Core for Gas Uptake and Tandem Detection of Iodide and Mercury. *ACS Appl. Mater. Interfaces* **2017**, *9*, 21438–21446. [[CrossRef](#)]
19. Hussain, S.; De, S.; Iyer, P.K. Thiazole-Containing Conjugated Polymer as a Visual and Fluorometric Sensor for Iodide and Mercury. *ACS Appl. Mater. Interfaces* **2013**, *5*, 2234–2240. [[CrossRef](#)]
20. Kanellis, V.G. Sensitivity limits of biosensors used for the detection of metals in drinking water. *Biophys. Rev.* **2018**, *10*, 1415–1426. [[CrossRef](#)]
21. Samanta, T.; Shunmugam, R. Colorimetric and fluorometric probes for the optical detection of environmental Hg (II) and As (III) ions. *Mater. Adv.* **2020**, *2*, 64–95. [[CrossRef](#)]
22. Ríos, M.C.; Bravo, N.F.; Sánchez, C.C.; Portilla, J. Chemosensors based on N-heterocyclic dyes: Advances in sensing highly toxic ions such as CN<sup>−</sup> and Hg<sup>2+</sup>. *RSC Adv.* **2021**, *11*, 34206–34234. [[CrossRef](#)] [[PubMed](#)]
23. Shang, L.; Dong, S.; Nienhaus, G.U. Ultra-small fluorescent metal nanoclusters: Synthesis and biological applications. *Nano Today* **2011**, *6*, 401–418. [[CrossRef](#)]
24. Saleh, S.; Ali, R.; Hirsch, T.; Wolfbeis, O.S. Detection of biotin–avidin affinity binding by exploiting a self-referenced system composed of upconverting luminescent nanoparticles and gold nanoparticles. *J. Nanoparticle Res.* **2011**, *13*, 4603–4611. [[CrossRef](#)]
25. Ghannay, S.; Bakari, S.; Ghabi, A.; Kadri, A.; Msaddek, M.; Aouadi, K. Stereoselective synthesis of enantiopure N -substituted pyrrolidin-2,5-dione derivatives by 1,3-dipolar cycloaddition and assessment of their in vitro antioxidant and antibacterial activities. *Bioorganic Med. Chem. Lett.* **2017**, *27*, 2302–2307. [[CrossRef](#)] [[PubMed](#)]
26. Ghannay, S.; Bakari, S.; Msaddek, M.; Vidal, S.; Kadri, A.; Aouadi, K. Design, synthesis, molecular properties and in vitro antioxidant and antibacterial potential of novel enantiopure isoxazolidine derivatives. *Arab. J. Chem.* **2020**, *13*, 2121–2131. [[CrossRef](#)]
27. Kadri, A.; Aouadi, K. In vitro antimicrobial and  $\alpha$ -glucosidase inhibitory potential of enantiopure cycloalkylglycine derivatives: Insights into their in silico pharmacokinetic, druglikeness, and medicinal chemistry properties. *J. Appl. Pharm. Sci.* **2020**, *10*, 107–115.
28. Ghabi, A.; Brahmi, J.; Alminderej, F.; Messaoudi, S.; Vidal, S.; Kadri, A.; Aouadi, K. Multifunctional isoxazolidine derivatives as  $\alpha$ -amylase and  $\alpha$ -glucosidase inhibitors. *Bioorganic Chem.* **2020**, *98*, 103713. [[CrossRef](#)] [[PubMed](#)]
29. Aouadi, K.; Jeanneau, E.; Msaddek, M.; Praly, J.-P. 1,3-Dipolar cycloaddition of a chiral nitron to (E)-1,4-dichloro-2-butene: A new efficient synthesis of (2S,3S,4R)-4-hydroxyisoleucine. *Tetrahedron Lett.* **2012**, *53*, 2817–2821. [[CrossRef](#)]
30. Cordero, F.M.; Pisaneschi, F.; Goti, A.; Ollivier, J.; Salaün, J.; Brandi, A. New Synthesis of  $\beta$ -Lactams by Ethylene Extrusion from Spirocyclopropane Isoxazolidines. *J. Am. Chem. Soc.* **2000**, *122*, 8075–8076. [[CrossRef](#)]
31. Abda, H.; Aouadi, K.; Perrin, L.; Msadek, M.; Praly, J.-P.; Vidal, S. Stereoselective synthesis of enantiopure cycloalkylglycines by 1, 3-dipolar cycloaddition of a chiral nitron to cycloalkenes. *Eur. J. Org. Chem.* **2014**, *27*, 6017–6024. [[CrossRef](#)]
32. Seerden, J.-G.; Boeren, M.M.M.; Scheeren, H.W. 1,3-Dipolar cycloaddition reactions of nitrones with alkyl vinyl ethers catalyzed by chiral oxazaborolidines. *Tetrahedron* **1997**, *53*, 11843–11852. [[CrossRef](#)]
33. Elshaarawy, R.F.; Ali, R.; Saleh, S.M.; Janiak, C. A novel water-soluble highly selective “switch-on” ionic liquid-based fluorescent chemi-sensor for Ca(II). *J. Mol. Liq.* **2017**, *241*, 308–315. [[CrossRef](#)]
34. Ali, R.; Saleh, S.M.; Elshaarawy, R.F.M. Turn-on pH nano-fluoresensor based on imidazolium salicylaldehyde ionic liquid-labeled silica nanoparticles. *RSC Adv.* **2016**, *6*, 86965–86975. [[CrossRef](#)]
35. Saleh, S.M.; Ali, R.; Hegazy, M.E.F.; Alminderej, F.M.; Mohamed, T.A. The natural compound chrysosplenol-D is a novel, ultrasensitive optical sensor for detection of Cu (II). *J. Mol. Liq.* **2020**, *302*, 112558. [[CrossRef](#)]
36. Saleh, S.M.; Alminderej, F.M.; Ali, R.; Abdallah, O.I. Optical sensor film for metribuzin pesticide detection. *Spectrochim. Acta Part A Mol. Biomol. Spectrosc.* **2020**, *229*, 117971. [[CrossRef](#)]
37. Ali, R.; Ali, I.A.; Messaoudi, S.; Alminderej, F.M.; Saleh, S.M. An effective optical chemosensor film for selective detection of mercury ions. *J. Mol. Liq.* **2021**, *336*, 116122. [[CrossRef](#)]
38. Ali, R.; Alminderej, F.M.; Messaoudi, S.; Saleh, S.M. Ratiometric ultrasensitive optical chemisensor film based antibiotic drug for Al (III) and Cu (II) detection. *Talanta* **2021**, *221*, 121412. [[CrossRef](#)]
39. Ali, R.; Elshaarawy, R.F.; Saleh, S.M. Turn-on ratiometric fluorescence sensor film for ammonia based on salicylaldehyde-ionic liquid. *J. Environ. Chem. Eng.* **2017**, *5*, 4813–4818. [[CrossRef](#)]
40. Thakur, A.; Mandal, D.; Deb, P.; Mondal, B.; Ghosh, S. Synthesis of triazole linked fluorescent amino acid and carbohydrate bio-conjugates: A highly sensitive and skeleton selective multi-responsive chemosensor for Cu (II) and Pb (II)/Hg (II) ions. *RSC Adv.* **2014**, *4*, 1918–1928. [[CrossRef](#)]
41. Saleh, S.M.; Ali, R.; Elshaarawy, R.F.M. A ratiometric and selective fluorescent chemosensor for Ca (II) ions based on a novel water-soluble ionic Schiff-base. *RSC Adv.* **2016**, *6*, 68709–68718. [[CrossRef](#)]

42. Saleh, S.M.; El-Sayed, W.A.; El-Manawaty, M.A.; Gassoumi, M.; Ali, R. An Eco-Friendly Synthetic Approach for Copper Nanoclusters and Their Potential in Lead Ions Sensing and Biological Applications. *Biosensors* **2022**, *12*, 197. [[CrossRef](#)]
43. Ali, R.; Alfeneekh, B.; Chigurupati, S.; Saleh, S.M. Green synthesis of pregabalin-stabilized gold nanoclusters and their applications in sensing and drug release. *Arch. der Pharm.* **2022**, *355*, e2100426. [[CrossRef](#)]
44. Saleh, S.M.; Ali, R.; Alminderej, F.; Ali, I.A.I. Ultrasensitive Optical Chemosensor for Cu(II) Detection. *Int. J. Anal. Chem.* **2019**, *2019*, 1–8. [[CrossRef](#)]
45. Saleh, S.M.; Almotiri, M.K.; Ali, R. Green synthesis of highly luminescent gold nanoclusters and their application in sensing Cu(II) and Hg(II). *J. Photochem. Photobiol. A: Chem.* **2022**, *426*, 113719. [[CrossRef](#)]
46. Saleh, S.M.; Elkady, E.M.; Ali, R.; Alminderej, F.; Mohamed, T.A. Novel chemical sensor for detection Ca(II) ions based on ferutinin. *Spectrochim. Acta Part A Mol. Biomol. Spectrosc.* **2018**, *205*, 264–268. [[CrossRef](#)]
47. Saleh, S.M.; El-Sayed, W.A.; El-Manawaty, M.A.; Gassoumi, M.; Ali, R. Microwave-Assisted Rapid Synthesis of Luminescent Tryptophan-Stabilized Silver Nanoclusters for Ultra-Sensitive Detection of Fe (III), and Their Application in a Test Strip. *Biosensors* **2022**, *12*, 425. [[CrossRef](#)]
48. Kaewtong, C.; Niamsa, N.; Wannoo, B.; Morakot, N.; Pulpoka, B.; Tuntulani, T. Optical chemosensors for Hg<sup>2+</sup> from terthiophene appended rhodamine derivatives: FRET based molecular and in situ hybrid gold nanoparticle sensors. *New J. Chem.* **2014**, *38*, 3831–3839. [[CrossRef](#)]
49. Luo, J.; Jiang, S.; Qin, S.; Wu, H.; Wang, Y.; Jiang, J.; Liu, X. Highly sensitive and selective turn-on fluorescent chemosensor for Hg<sup>2+</sup> in pure water based on a rhodamine containing water-soluble copolymer. *Sensors Actuators B Chem.* **2011**, *160*, 1191–1197. [[CrossRef](#)]
50. Madhu, S.; Sharma, D.K.; Basu, S.K.; Jadhav, S.; Chowdhury, A.; Ravikanth, M. Sensing Hg(II) in Vitro and in Vivo Using a Benzimidazole Substituted BODIPY. *Inorg. Chem.* **2013**, *52*, 11136–11145. [[CrossRef](#)]
51. Liu, J.; Yu, M.; Wang, X.C.; Zhang, Z. A highly selective colorimetric sensor for Hg<sup>2+</sup> based on nitrophenyl-aminothiourea. *Spectrochim. Acta Part A Mol. Biomol. Spectrosc.* **2012**, *93*, 245–249. [[CrossRef](#)] [[PubMed](#)]
52. Dai, H.; Liu, F.; Gao, Q.; Fu, T.; Kou, X. A highly selective fluorescent sensor for mercury ion (II) based on azathia-crown ether possessing a dansyl moiety. *Luminescence* **2011**, *26*, 523–530. [[CrossRef](#)] [[PubMed](#)]
53. El-Shekheby, H.A.; Mangood, A.H.; Hamza, S.M.; Al-Kady, A.S.; Ebeid, E.Z.M. A highly efficient and selective turn-on fluorescent sensor for Hg<sup>2+</sup>, Ag<sup>+</sup> and Ag nanoparticles based on a coumarin dithioate derivative. *Luminescence* **2014**, *29*, 158–167. [[CrossRef](#)] [[PubMed](#)]
54. Wang, H.-F.; Wu, S.-P. Highly selective fluorescent sensors for mercury(II) ions and their applications in living cell imaging. *Tetrahedron* **2013**, *69*, 1965–1969. [[CrossRef](#)]
55. Praveen, L.; Babu, J.; Reddy, M.L.P.; Varma, R.L. Unfolding with mercury: Anthracene-oxyquinoline dyad as a fluorescent indicator for Hg (II). *Tetrahedron Lett.* **2012**, *53*, 3951–3954. [[CrossRef](#)]
56. Choi, J.; Lee, S.K.; Bae, J.; Chang, S.-K. Colorimetric signaling of Hg<sup>2+</sup> ions by a nitrobenzoxadiazole-appended cyclen-triester. *Tetrahedron Lett.* **2014**, *55*, 5294–5297. [[CrossRef](#)]
57. Frisch, M.J.; Trucks, G.W.; Schlegel, H.B.; Scuseria, G.E.; Robb, M.A.; Cheeseman, J.R.; Montgomery, J.A., Jr.; Vreven, T.K.K.N.; Kudin, K.N.; Burant, J.C.; et al. *Gaussian 09, Revision D.01*; Gaussian, Inc.: Wallingford, CT, USA, 2013.
58. Wang, J.; Liu, Q.; Yang, D. Theoretical insights into excited-state hydrogen bonding effects and intramolecular proton transfer (ESIPT) mechanism for BTS system. *Sci. Rep.* **2020**, *10*, 5119. [[CrossRef](#)]
59. Figgen, D.; Rauhut, G.; Dolg, M.; Stoll, H. Energy-consistent Pseudopotentials for Group 11 and 12 Atoms: Adjustment to Multi-configuration Dirac–Hartree–Fock Data. *Chem. Phys.* **2005**, *311*, 227–244. [[CrossRef](#)]
60. Peterson, K.A.; Puzzarini, C. Systematically convergent basis sets for transition metals. II. Pseudopotential-based correlation consistent basis sets for the group 11 (Cu, Ag, Au) and 12 (Zn, Cd, Hg) elements. *Theor. Chim. Acta* **2005**, *114*, 283–296. [[CrossRef](#)]